2026 IEEE International Conference on Robotics and Automation (ICRA 2026)
June 1-5, 2026. Vienna, Austria

Automated retinal photocoagulation using instrument-integrated OCT and laser pattern mapping

Marius Briel[1,2], Ludwig Haide[1], Dongyue Wu[1,3], Justus Hornstein[4], Philipp Matten[1], Nicola Piccinelli[5]
Gernot Kronreif[6], Eleonora Tagliabue[1], Franziska Mathis-Ullrich[2]

***Abstract*— Retinal endolaser photocoagulation (REPC) is a repetitive intraocular surgical procedure that could greatly benefit from automation and distance-based control, improving both efficiency and safety. This work presents a robotic system designed for automated REPC, utilizing instrument-integrated optical coherence tomography (iiOCT) to facilitate real-time distance measurements. The system employs intraoperative spherical and ellipsoidal retinal models to convert 2D laser patterns into 3D arrangements, which are further refined through a control loop that incorporates online feedback. Ex vivo experiments in porcine eyes demonstrated clinical-level accuracy, with lateral and axial errors of $44\,\mu m$ and $29\,\mu m$, respectively. Additionally, the proposed mapping technique produced patterns with greater equidistance than baseline methods. This system showcases the potential to automate repetitive surgical tasks while maintaining the surgeon's control over critical decision-making processes in ophthalmic surgery.**

I. Introduction

Retinal microsurgery is a highly specialized field requiring exceptional precision due to the delicate nature of retinal tissues. These procedures require superior hand-eye coordination and fine motor control that surpasses the limits of untrained individuals [1], [2]. Despite advancements in stereo microscopy, surgeons often struggle to accurately estimate instrument-to-retina distances when relying solely on visual cues [3]. Surgical robots offer significant advantages, including enhanced positioning accuracy through motion scaling, tremor reduction, and the ability to maintain steady instrument states [4]. By automating repetitive tasks, robotic systems can reduce cognitive load, allowing surgeons to focus on higher-level decision-making [5].

Retinal endolaser photocoagulation (REPC), commonly used to treat conditions like retinal detachments or diabetic retinopathy, is an ideal candidate for automation. REPC employs an optical fiber–integrated endolaser probe to deliver laser energy to the retina, inducing localized thermal tissue alteration that destroys abnormal blood vessels or seals retinal breaks [6]. The downsides of manual operation include the difficulty of controlling distance, which is crucial for safety and effective treatment, and the repetitiveness of the procedure, which requires surgeons to maintain prolonged focus. With up to 1500 panretinal laser spots applied over 30 minutes [7], robotic assistance could significantly improve efficiency and precision.

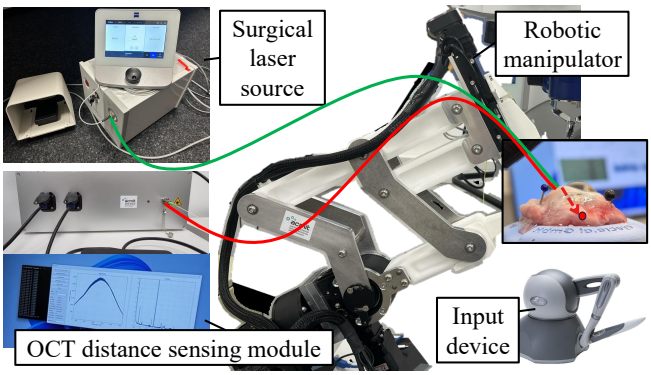

Fig. 1: The experimental setup comprises a robotic manipulator, an optical coherence tomography (OCT)-based sensing module, and a surgical laser source. The probe integrates two optical fibers for distance sensing and laser delivery

This work leverages a teleoperated system [8] to enable automated REPC. The system utilizes instrument-integrated optical coherence tomography (iiOCT) for intraocular distance measurement and retinal surface modeling. Intraoperative spherical and ellipsoidal models are employed to map 2D laser patterns onto 3D retinal surfaces for optimal pattern placement. It is challenging to map 2D patterns onto 3D shapes while preserving the relative distances within the pattern. However, equidistant laser patterns are essential for uniform energy distribution on the retina, preventing both over- and undertreatment [9]. A control loop based on iiOCT feedback dynamically adjusts the surgical plan to maintain safe and consistent instrument-to-retina distances, even under high-speed operation. The system's performance is validated through simulations and ex vivo experiments on open-sky and closed-sky porcine eyes (Fig. 1).

II. Related work

Robotic systems in ophthalmic surgery encompass handheld, magnetic, and telemanipulated platforms [5]. Notable examples are Micron [10], OctoMag [11], and RAMIS ophthalmic micromanipulator [12]. Handheld instruments integrate motors to compensate for unintended micro-

[1] Carl Zeiss AG, 73447 Oberkochen, Germany: marius.briel@zeiss.com
[2] Laboratory for Surgical Planning and Robotic Cognition (SPARC), Friedrich-Alexander-University Erlangen-Nürnberg, Germany: franziska.mathis-ullrich@fau.de
[3] Department of Microsystems Engineering, University of Freiburg, Germany
[4] Karlsruhe Institute of Technology, Germany
[5] Department of Engineering for Innovation Medicine, Università di Verona, Italy
[6] Austrian Center of Medical Innovation and Technology (ACMIT), Wiener Neustadt, Austria

movements [10]. Magnetic systems utilize electromagnetic fields to control microrobots or flexible instruments [11]. Telemanipulated systems allow remote control of robotic manipulators via input devices [12].

Balicki et al. first integrated fiber-based OCT into a microsurgical instrument held by a Cartesian coordinate robot, enabling safety constraints and constant distance maintenance [13]. More recently, Piccinelli et al. developed an OCT-enhanced multi-modal feedback platform for robot-assisted ophthalmic surgery, incorporating haptic, visual, and acoustic feedback [8]. Furthermore, they used a radial basis function model to define a safety band [14]. Prior work used real-time iiOCT data to regulate the distance between the surgical instrument tip and the retina during REPC surgery, with a pilot study demonstrating a $59\,\%$ reduction in surgeon workload [15].

Initial attempts to automate REPC have utilized handheld and magnetic robotic systems with camera feedback. Yang et al. employed the handheld Micron system for automated intraocular laser surgery, using high-resolution optical motion tracking to determine instrument tip poses [16]. Planar movements were contolled via microscope-based visual servoing, while axial movements maintained a constant distance from the retina [17]. However, Micron's limited motion range of $4\,\mathrm{mm}$ restricts its application to specific areas, such as retinal break treatments [18]. Additional challenges such as camera calibration, 3D reconstruction, and zoom optics further complicate automation [19].

An automated large-range panretinal photocoagulation system was presented by Charreyron et al. [20], featuring a magnetically steered endolaser probe. Their experiments were conducted on a spherical phantom eye. Pattern planning, however, relied on 2D images from a monoscopic camera and the 3D topology of the retinal surface was negelected. Distortions from eye optics and wide-angle viewing systems further complicate modeling.

In summary, surgical robotic systems have been utilized for perception and control in REPC; however, automating patterned laser delivery in closed-sky scenarios remains unresolved. Robotic systems relying on extraocular sensors are particularly affected by distortions and limited depth perception, which hinder validation in realistic closed-sky settings. In contrast, intraocular iiOCT avoids these distortions and enables precise 3D reconstruction of closed-sky eye geometry by integrating robotic instrument poses with distance measurements [21]. This work exploits the unique advantages of iiOCT to improve robot-assisted laser surgery.

III. Methods

A. Surgical workflow

To facilitate collaboration between automated components and surgeons, our approach delegates critical decisions to surgeons while automating repetitive surgical steps (Fig. 2). After vitrectomy (*S1*), surgeons navigate the endolaser probe to the pathologic area using an input device and select the laser pattern by specifying its shape, spacing, and size (*S2*). After automated pattern delivery, surgeons visually assess

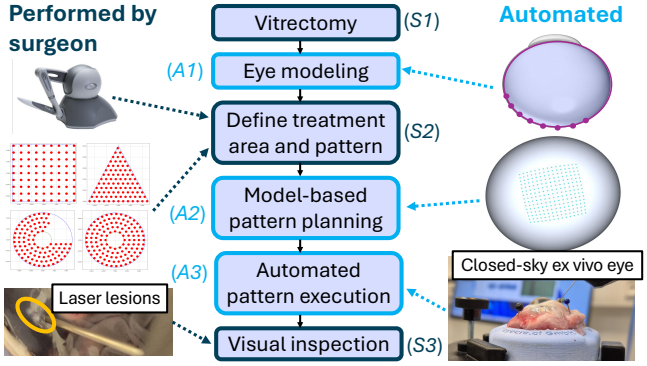

Fig. 2: Automated REPC workflow

the outcome and, if necessary, make adjustments via the input device (*S3*). The automated system comprises two main components: The planning unit determines target laser locations (*A2*) on the eye model (*A1*), while the control unit manages real-time data processing and motion execution (*A3*).

B. Eye modeling

The iiOCT engine acquires one-dimensional tomographic scans (A-scans) of the retinal structure. A convolutional neural network is used for real-time boundary segmentation in A-scans, enabling instrument-to-retina distance estimation [22]. However, a wash-out effect is observed in scans, characterized by poor visibility of the retina, and particularly pronounced at speeds above $3\,\mathrm{mm/s}$ in the axial direction. To address this issue, a distance correction pipeline is used [23], [24]. Using forward kinematics, these distances are converted to 3D points of the retinal surface, generating a point cloud as the probe moves, following the method in [8]. Alternatively, eye models could be based on registered preoperative data [25]. To address noise and non-uniformity in the reconstructed point clouds, intraoperative models are created. Spherical [26], [27] and ellipsoidal [28], [29] fitting methods are employed to represent the eye's shape for surgical planning. Ellipsoidal models, shown to outperform spherical models in accuracy [29], better capture variations in eye curvature along different axes. Nevertheless, spherical models were used due to their simplicity and computational efficiency. Furthermore, ellipsoid fitting exhibits unstable performance when provided with insufficient data points [28].

C. Sphere-based pattern planning

2D and 3D Euclidean distances can be misleading as they do not account for the retinal surface curvature. Fig. 3a illustrates a 2D mapping baseline method that neglects curvature effects. The great circle path computes the shortest distance between two surface points (r, λ_1, ϕ_1) and (r, λ_2, ϕ_2) along a sphere's surface. This path is defined by the intersection of the sphere with a plane through its center and the two surface points. The arc length d^{3D} is calculated using the

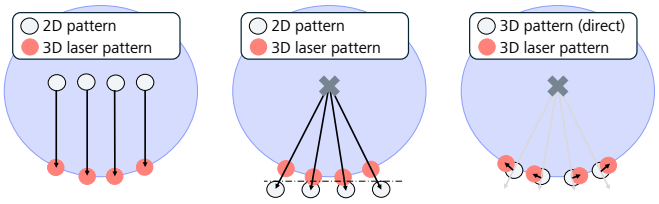

(a) 2D (b) Direct (c) Optimized

Fig. 3: Three model-based mappings of 2D patterns onto the 3D retinal surface

spherical law of cosines:

$$d^{3D} = r \arccos\left(\sin\phi_1 \sin\phi_2 + \cos\phi_1 \cos\phi_2 \cos(|\Delta\lambda|)\right), \quad (1)$$

where λ_1, λ_2 are longitudes and ϕ_1, ϕ_2 are latitudes. Direct mapping transfers a 2D pattern onto a sphere centered at $\mathbf{c}$ with radius r (Fig. 3b). The tangent plane of the pattern center $\mathbf{s} = (s_x, s_y, s_z)$ is spanned by

$$\mathbf{t}_1 = \frac{(\mathbf{s}-\mathbf{c}) \times \mathbf{v}}{\|(\mathbf{s}-\mathbf{c}) \times \mathbf{v}\|}, \quad \mathbf{t}_2 = \frac{(\mathbf{s}-\mathbf{c}) \times \mathbf{t}_1}{\|(\mathbf{s}-\mathbf{c}) \times \mathbf{t}_1\|}, \quad (2)$$

where $\mathbf{v}$ is a unit vector in the z-direction, which corresponds to the optical axis. The 2D pattern points $\{\mathbf{u}_i = (u_x, u_y)\}$ are mapped to the tangent plane as $\mathbf{p}_i = \mathbf{s} + u_x\mathbf{t}_1 + u_y\mathbf{t}_2$. These points are then projected onto the sphere's surface:

$$\mathbf{m}_i = \mathbf{c} + r \cdot \frac{\mathbf{p}_i - \mathbf{c}}{\|\mathbf{p}_i - \mathbf{c}\|}. \quad (3)$$

The directly mapped pattern $\{\mathbf{m}_i\}$ serves as an initial guess for optimization, which iteratively adjusts the mapping to minimize distortion, ensuring the mapped pattern retains its original equidistant relationships while conforming to the sphere's curvature. Given desired 2D distances $d_i^{2D} = ||\mathbf{p}_i - \mathbf{s}||$ and corresponding great-circle distances

$$d_i^{3D} = \text{GreatCircleDistance}(\mathbf{s}, \mathbf{m}_i; r, \mathbf{c}), \quad (4)$$

the goal is to optimize 3D pattern points $\mathbf{m}_i$ to preserve original 2D distances such that $d_i^{3D} \approx d_i^{2D}$ (Fig. 3c):

$$\arg\min \quad J(\alpha_i) = \arg\min \sum_i \left(d_i^{3D}(\alpha_i) - d_i^{2D}\right)^2, \quad (5)$$

with updates given by

$$\mathbf{m}_i' = \mathbf{c} + r \cdot \frac{\mathbf{s} + \alpha_i(\mathbf{m}_i - \mathbf{s}) - \mathbf{c}}{\|\mathbf{s} + \alpha_i(\mathbf{m}_i - \mathbf{s}) - \mathbf{c}\|}. \quad (6)$$

D. Ellipsoid-based pattern planning

Let the ellipsoid be centered at $\mathbf{c} = (c_x, c_y, c_z)$ with semi-axes r_1, r_2, and r_3. For accurate distance calculations on ellipsoids, we employ the Vincenty distance, commonly used in geodesics [30]. The pattern points $\mathbf{p}_i$ on the tangent plane are determined similarly to the sphere; however, to map $\mathbf{p}_i = (p_x, p_y, p_z)$ onto the ellipsoid, we require the factor

$$\frac{1}{k_i} = \sqrt{\left(\frac{p_x - c_x}{r_1}\right)^2 + \left(\frac{p_y - c_y}{r_2}\right)^2 + \left(\frac{p_z - c_z}{r_3}\right)^2}. \quad (7)$$

The direct mapping is then given by:

$$\mathbf{m}_i = \mathbf{c} + k_i \cdot (\mathbf{p}_i - \mathbf{c}). \quad (8)$$

The Vincenty distance between any two mapped points $\mathbf{m}_i$ and $\mathbf{m}_j$ on the ellipsoid is:

$$d_{ij}^{3D} = \text{VincentyDistance}(\mathbf{m}_i, \mathbf{m}_j; r_1, r_2, r_3, \mathbf{c}). \quad (9)$$

Our goal is to iteratively adjust the pattern so that its distances d_{ij}^{3D} closely resemble the target distances d_{ij}^{2D}. The objective function sums the squared differences between computed Vincenty and target distances:

$$f(\mathbf{m}_i, \mathbf{m}_j) = \sum_{i,j} \left(d_{ij}^{3D}(\mathbf{m}_i, \mathbf{m}_j) - d_{ij}^{2D}\right)^2. \quad (10)$$

To ensure conformity with the ellipsoidal equation, a penalty term $P(\mathbf{m}_i, \mathbf{m}_j)$ is added. The combined objective function $J = f + P$ is minimized using the gradient-based optimization algorithm L-BFGS (Limited-memory Broyden–Fletcher–Goldfarb–Shanno) [31], with the direct ellipsoid mapping serving as the initial guess.

E. Automated pattern execution

The end-effector poses for the planned laser pattern are computed by offsetting the optimized pattern points toward the remote center of motion (RCM). This working distance, along with the laser pulse parameters (power and duration), influences the energy density for each spot. To mitigate modeling errors, a feedback loop is implemented. Real-time iiOCT measurements dynamically refine the laser's working distance to maintain a constant distance throughout the treatment.

Three control modes are implemented, offering varying precision levels, at the cost of increased computational complexity. In *Mode 0*, robotic control operates solely on the precomputed model-based trajectory, applying a trapezoidal velocity profile with a quintic polynomial blend between consecutive end-effector poses. In *Mode 1*, proportional control is applied exclusively at the laser points, prioritizing fast execution but compromising overall instrument movement smoothness. In *Mode 2*, proportional control is extended to the entire trajectory, ensuring consistent instrument-to-retina distances at all times. An illustration of the different modes is provided in Fig. 4.

IV. Experimental Validation

A. Experimental setup

The robot (*ACMIT, Wiener Neustadt, Austria*) is a three-degree-of-freedom manipulator with a parallel kinematic structure providing a mechanical RCM. The pivoting range is $\pm 40°$ for both rotating axes around the RCM, with a linear insertion range of $100\,\text{mm}$ [8]. It supports position-based control at $50\,\text{Hz}$. The Phantom Omni (*SensAble, USA*) serves as the input device for end-effector control. A distance sensing module, developed for intraocular measurements, utilizes OCT for precise distance estimation, based on a common-path spectral domain OCT configuration with $12.8\,\text{mm}$ imaging depth in air [8].

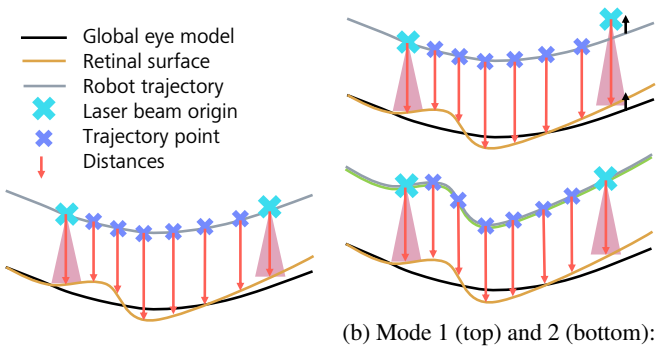

(a) Mode 0: Model-based only

(b) Mode 1 (top) and 2 (bottom): Sensor-based depth adjustment

Fig. 4: Three control modes offering varying levels of precision in maintaining desired instrument-to-retina distances

Eye	Condition	Direction	Evaluation	Display
1	closed-sky	lateral	mappings	Table II, Fig. 8
2	open-sky	lateral	detachment	Fig. 9, Fig.10
3	open-sky	axial	modes	Fig. 11
4	open-sky	axial	movement time	Table III

TABLE I: Overview of porcine eyes used in real-world experiments

The ZEISS VISULAS® green (*Carl Zeiss Meditec AG, Jena, Germany*) surgical laser source operates at 532 nm with a maximum output of 1.5 W. Automation is achieved via an ARDUINO MEGA 2560 for software-based laser triggering, eliminating the need for a foot switch. A dual-fiber probe was developed for distance-controlled REPC. It integrates a single-mode OCT sensing fiber (*SM 780HP, Diamond*) with an 842 µm gold-coated GRIN fiber (*YOFC*) at its tip for common-path OCT sensing, alongside a 50 µm core multi-mode fiber (*FG050LGA, Thorlabs*) for surgical laser delivery. Both fibers, with diameters of 125 µm and 250 µm, are housed in a stainless steel tube (OD: 0.65 mm, ID: 0.49 mm) using medical-grade epoxy (*4305 LC, Loctite*). An overview of the surgical setup is shown in Fig. 1.

B. Experimental procedure

Experiments are conducted on four ex vivo porcine eyes, and Table I provides an overview of the porcine eyes used for quantitative evaluation. In the closed-sky configuration, instruments are inserted through a trocar, and the RCM is aligned with it; in the open-sky condition, the eye is dissected. In both cases, the eyes are fixed on a platform and remain static within the robot's coordinate system. An initial OCT spiral scan is performed to obtain a sphere fit of the retina for surgical planning. Laser patterns are sized and spaced between 7×7 to 15×15, and 400 µm to 800 µm, respectively, similar to [9]. During pattern execution, iiOCT distance data, robotic poses, and laser timestamps are recorded for evaluation. For quantitative evaluation in closed-sky eyes, great-circle paths are computed. For open-sky eyes, a high-resolution grid scan (10 µm spacing) is performed for geodesic distance computation using a radial

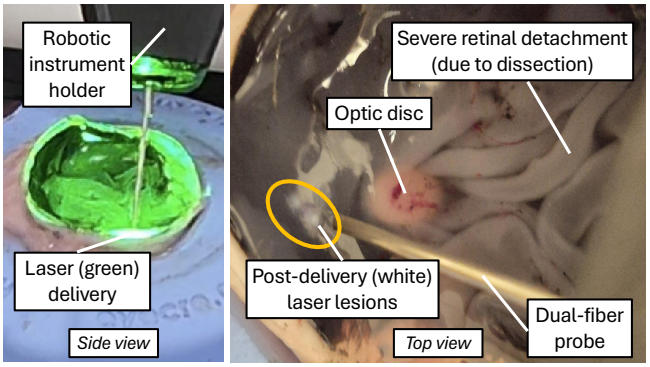

Fig. 5: Automated REPC using a probe that integrates laser and sensing fibers on an open-sky porcine eye

basis functions surface model [21]. This was done due to the increased surface irregularity of open-sky eyes, which we considered to resemble pathological eyes with retinal detachments. A fiber-integrated cannula without a laser fiber is used to improve signal quality. Laser delivery locations are reconstructed with distance measurements and forward kinematics, projecting delivery locations onto the model in the probe's axial direction to account for online measurement errors. A proof of concept with the dual-fiber probe is demonstrated on an open-sky porcine eye (Fig. 5).

C. Metrics

Previous studies established a ground truth for lateral evaluation of laser delivery through overlays in the microscopic view [16], [20]. However, these 2D overlays do not account for 3D retinal geometry. Thus, we assess distortions in equidistant spacing introduced by 2D-to-3D mapping [9]. We compute Euclidean distances $d_{2D(i,j)}$ in the 2D pattern and geodesic distances $d_{3D(i,j)}$ in the delivered pattern. The (global) mean absolute distortion (MAD) is defined as:

$$\mathrm{MAD}[\%] = \frac{1}{n(n-1)} \sum_{i=1}^{n} \sum_{\substack{j=1 \\ j \neq i}}^{n} \left| \frac{d_{3D(i,j)}}{d_{2D(i,j)}} - 1 \right| , \tag{11}$$

where n is the number of points in the pattern (e.g., 225 for a 15×15 pattern). The maximum absolute distortion (MaxAD) is defined as:

$$\mathrm{MaxAD}[\%] = \max \left| \frac{d_{3D(i,j)}}{d_{2D(i,j)}} - 1 \right| . \tag{12}$$

The local metric exclusively considers immediate neighbors (i', j'):

$$\mathrm{MAD}[\mu\mathrm{m}] = \frac{1}{4\sqrt{n}(\sqrt{n}-1)} \sum_{(i',j')} \left| d_{3D(i',j')} - d_{2D(i',j')} \right| . \tag{13}$$

The (global) mean signed distortion (MSD) is defined as:

$$\mathrm{MSD}[\%] = \frac{1}{n(n-1)} \sum_{i=1}^{n} \sum_{\substack{j=1 \\ j \neq i}}^{n} \frac{d_{3D(i,j)}}{d_{2D(i,j)}} - 1 , \tag{14}$$

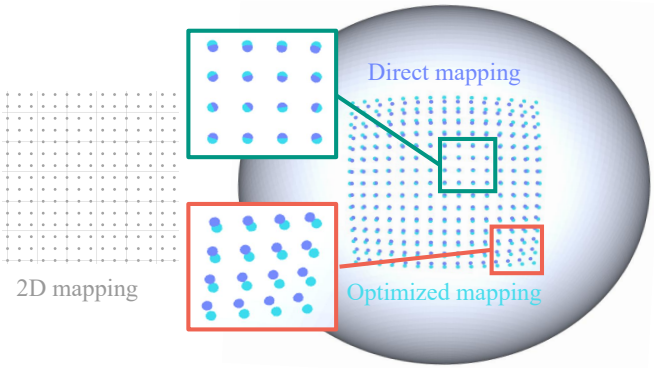

Fig. 6: Direct and optimized 3D mapping for a 15×15 pattern

with corresponding standard deviation (SD):

$$\mathrm{SD}[\%] = \sqrt{\frac{1}{n(n-1)} \sum_{\substack{i,j=1 \\ j\neq i}}^{n} \left(\frac{d_{3D(i,j)}}{d_{2D(i,j)}} - 1 - \mathrm{MSD}\right)^2}. \quad (15)$$

Local MSD[µm] and SD[µm] are defined similarly, but focusing on immediate neighbors (i', j').

Axial control accuracy is evaluated by measuring absolute deviations from the target distance, set at 5 mm. The metrics used are referred to as mean absolute error (MAE) and maximum absolute error (MaxAE). To ensure consistent laser spot sizes, axial accuracy at laser triggering is especially critical. Accordingly, MAE-L and MaxAE-L are defined to quantify errors specifically at those locations.

V. Results

A. Simulation results

Robot Operating System Visualization (RViz) is used for sub-system testing of pattern mapping. Fig. 6 shows the behavior of mapping methods for a 15×15 pattern. The 2D mapping overestimates distances due to unaccounted eye curvature, while direct mapping underestimates them. Fig. 7 illustrates ellipsoid-based pattern mapping distortions on an ellipsoid fit of the Lankenau model eye (*Modell-Augen Manufaktur Dr. Eva Lankenau, Germany*), with semi-axes of 9.35 mm, 9.16 mm, and 8.62 mm. The optimized mapping method maintains the MAD below 0.6 %, even for larger patterns, with a maximum MaxAD of 4.9 % for a 15×15 pattern – a 70 % reduction compared to direct mapping.

Differences between sphere-based and ellipsoid-based optimized mappings increase with pattern size. For the 15×15 pattern, the ellipsoid-based MAD is 0.29 %, while the sphere-based is 3.2 %. The MaxADs are 4.9 % and 13.4 %, respectively, highlighting the importance of eye model choice for accuracy. An ellipsoidal model reduces mapping distortions when an accurate fit is available.

B. Lateral accuracy analysis in porcine eyes

Table II presents the MSD and SD in the closed-sky experiment, comparing mapping methods for a 15×15 pattern with 800 µm spacing. Direct mapping leads to overly dense placement (MSD of $-8.11\,\%$ and $-57.6\,\mu\mathrm{m}$), while

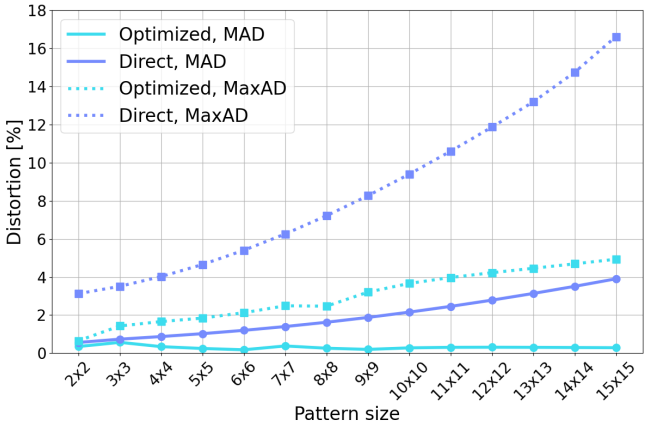

Fig. 7: Direct and optimized ellipsoid-based pattern mapping distortions for various pattern sizes with 400 µm spacing

TABLE II: Mean distortions (MSD) and standard deviations of distortions (SD) of direct and optimized mapping compared to 2D mapping

15×15, 800 µm	Global		Local	
	MSD	SD	MSD	SD
2D mapping	3.29 %	5.34 %	60.7 µm	70.2 µm
Direct mapping	−8.11 %	5.84 %	−57.6 µm	81.2 µm
Optimized mapping	−1.66 %	4.98 %	9.71 µm	67.0 µm

2D mapping leads to insufficient coverage (MSD of 3.29 % and 60.7 µm). Optimized mapping achieves minimal MSD of −1.66 % and 9.71 µm, with the lowest SD of 4.98 % and 67.0 µm. Results align with qualitative observations in Fig. 6. The evaluated optimized 15×15 laser pattern, along with its corresponding points projected on the sphere, are shown in Fig. 8. These projections are used to compute great-circle paths, forming the foundation for evaluation. The minimal deviation observed between the delivered laser points and their projections supports the suitability of using a sphere within a closed-sky eye.

Fig. 9 shows global optimized pattern distortions in an open-sky porcine eye. The significant retinal detachment due to post-mortem degradation and dissection results in a MAD of 14 % and a MaxAD of 30 %. Laser points of the 7×7 pattern show greater accuracy on smoother retinal areas, while distortions are more pronounced in irregular regions due to large geodesic distances compared to the smooth spherical eye model.

Fig. 10 displays signed deviations from the target spacing of 400 µm for a 7×7 pattern. Considering only direct neighbors, the MAD and MaxAD reduce to 11 % and 25 %, respectively, with a maximum spacing of 499 µm and a mean absolute deviation of 44 µm. The minimum spacing of 395 µm indicates negligible overlapping between laser spots.

C. Axial accuracy analysis in porcine eyes

Fig. 11 shows control mode performance with a suboptimal sphere fit of a porcine eye. In Mode 0, the instrument-

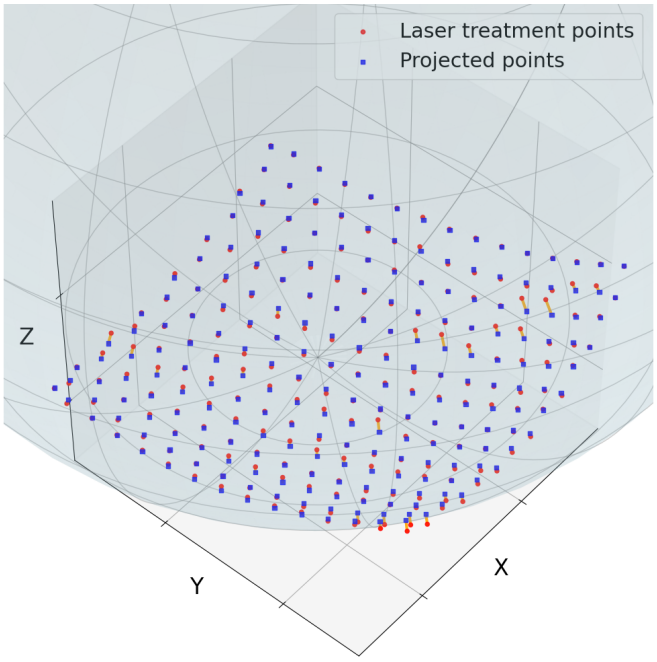

Fig. 8: A 15×15 optimized laser pattern delivered within a closed-sky porcine retina, alongside the points projected onto a fitted sphere

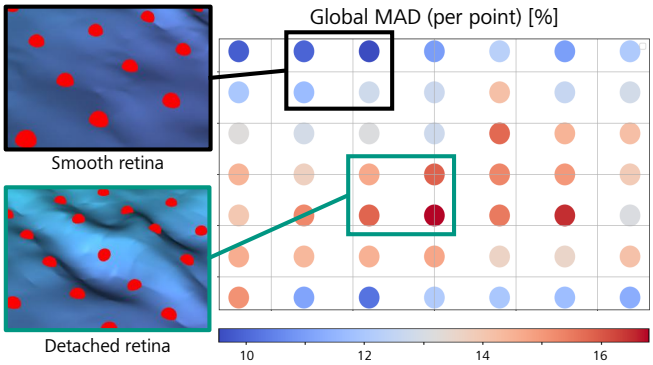

Fig. 9: Color-coded distortions per laser point in an open-sky porcine eye with retinal detachment

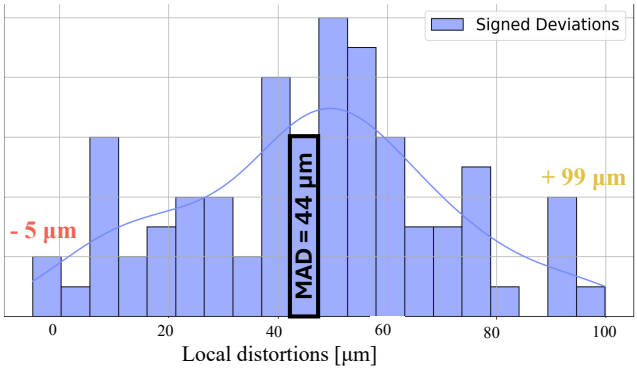

Fig. 10: Signed deviations from the target spacing of $400\,\mu\text{m}$ for a real-world 7×7 pattern

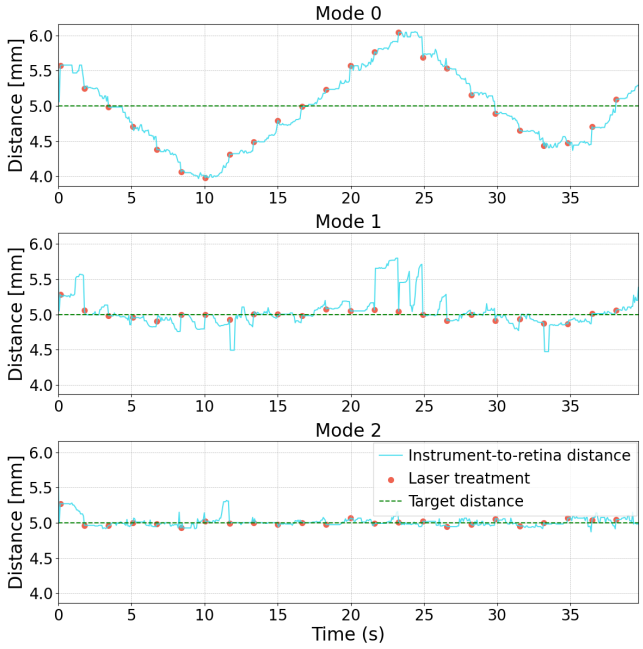

Fig. 11: Performance of various control modes with a sub-optimal sphere fit in an open-sky porcine eye

Movement time	MAE-L	MAE	MaxAE-L	MaxAE
Fast (0.1 s)	37	74	216	439
Medium (0.4 s)	29	60	72	376
Slow (0.9 s)	27	49	91	230

TABLE III: Axial deviations from the target instrument-to-retina distance of $5\,\text{mm}$ for Mode 2 at varying lateral movement durations between laser spots

to-retina distance is dictated by the inaccurate model. In Mode 1, online measurements at laser spots ensure consistent laser delivery. Mode 2 maintains constant distance throughout, regardless of surface irregularities.

Table III presents average and maximum axial deviations from target distances across different lateral movement times. The MAE-L improves by $10\,\mu\text{m}$ with slower movement, and MaxAE-L improves substantially with slower movements. The MAE of $74\,\mu\text{m}$ for fast movements is still below the level of surgeons' hand tremors [1].

VI. Discussion

The results of 2D-to-3D pattern mapping show a clear trend: as pattern size increases, optimized approaches increasingly outperform 2D and direct mapping. Utilizing ellipsoid fitting for the human eye's ellipsoidal shape [32] is beneficial for maintaining desired spacing on the retina. However, practical scenarios introduce system errors from various sources, including mechanical inaccuracies, sensor inaccuracies, and system latencies. Sphere-based experiments demonstrate precise lateral placement of laser points, with maximum errors within safety margins of $100\,\mu\text{m}$. Local model-based geodesic distances between laser points

are generally larger than the sphere-based distances used for planning. In vivo eyes are expected to have smoother curvatures than the open-sky porcine eyes, which exhibit significant retinal detachment. However, the in vivo transfer of our method may be affected by eye movements or tissue elasticity, both of which could impact the rigidity of the robotic system. Further work must incorporate movement compensation and dynamic modeling.

Given the optical fiber diameters, the lateral offset between the two fibers is considerable, especially with a target spot spacing of $400\,\mu\mathrm{m}$. Thus, the control algorithm must account for this lateral offset when using a dual-fiber probe. Future work could involve modifying the dual-fiber assembly to couple surgical laser and OCT signals into one fiber. Additionally, straight and rigid probes struggle to reach peripheral regions of the eye, indicating a need for curved/flexible probes [33]. The added degrees of freedom for bending and rotation complicate trajectory planning and control, though they could be modeled using the method described by Caravaca-Mora et al. [34].

VII. Conclusion

This study presented an automated robotic system that utilizes iiOCT for undistorted intraocular sensing, enabling precise automated laser pattern delivery in REPC procedures. Validation conducted in both open-sky and closed-sky environments demonstrated that the 2D-to-3D pattern mapping approach effectively preserved the desired 2D spatial relationships within a 3D context. By integrating automated pattern execution with precise distance control, the proposed system can enhance both the efficiency and safety of ocular laser surgery.

Acknowledgment

This work was supported by the European Union's Horizon Europe research and innovation programme under grant agreement N° 101070443. GEYEDANCE: AI Guidance for Robot-Assisted Eye Surgery.

References

[1] C. N. Riviere, R. S. Rader, and P. K. Khosla, "Characteristics of hand motion of eye surgeons," in *Proceedings of the 19th Annual International Conference of the IEEE Engineering in Medicine and Biology Society*, 1997, pp. 1690–1693. DOI: 10.1109/IEMBS.1997.757046.

[2] T. H. Williamson, *Vitreoretinal surgery*. Springer, 2021. DOI: 10.1007/978-3-030-68769-4.

[3] E. Z. Ahronovich, N. Simaan, and K. Joos, "A review of robotic and OCT-aided systems for vitreoretinal surgery," *Advances in Therapy*, vol. 38, pp. 2114–2129, 2021. DOI: 10.1007/s12325-021-01692-z.

[4] H. Mi, R. E. MacLaren, and J. Cehajic-Kapetanovic, "Robotising vitreoretinal surgeries," *Eye*, 2024. DOI: 10.1038/s41433-024-03149-3.

[5] E. Vander Poorten, C. N. Riviere, J. J. Abbott, *et al.*, "36 - Robotic retinal surgery," in *Handbook of Robotic and Image-Guided Surgery*, 2020, pp. 627–672. DOI: 10.1016/B978-0-12-814245-5.00036-0.

[6] M. Kaschke, K.-H. Donnerhacke, and M. S. Rill, Eds., *Optical Devices in Ophthalmology and Optometry*. 2014. DOI: 10.1002/9783527648962.

[7] F. Kuhn, *Vitreoretinal Surgery: Strategies and Tactics*. Springer, 2016. DOI: 10.1007/978-3-319-19479-0.

[8] N. Piccinelli, L. Haide, M. Briel, *et al.*, "GEYEDANCE: An OCT-enhanced multi-modal feedback platform for robot-assisted ophthalmic surgery," *IEEE Transactions on Medical Robotics and Bionics*, vol. 7, no. 3, pp. 1017–1028, 2025. DOI: 10.1109/TMRB.2025.3583133.

[9] K. Nishida, K. Miura, H. Sakaguchi, *et al.*, "The impact of spot size, spacing, pattern, duration and intensity of burns on the photocoagulation index in a geometric simulation of pan-retinal laser photocoagulation," *Acta Ophthalmologica*, vol. 97, no. 4, pp. 551–558, 2019. DOI: 10.1111/aos.13939.

[10] R. A. MacLachlan, B. C. Becker, J. C. Tabarés, G. W. Podnar, L. A. Lobes, and C. N. Riviere, "Micron: An actively stabilized handheld tool for microsurgery," *IEEE Transactions on Robotics*, vol. 28, no. 1, pp. 195–212, 2012. DOI: 10.1109/TRO.2011.2169634.

[11] M. P. Kummer, J. J. Abbott, B. E. Kratochvil, R. Borer, A. Sengul, and B. J. Nelson, "OctoMag: An electromagnetic system for 5-DOF wireless micromanipulation," *IEEE Transactions on Robotics*, vol. 26, no. 6, pp. 1006–1017, 2010. DOI: 10.1109/TRO.2010.2073030.

[12] M. A. Nasseri, M. Eder, S. Nair, *et al.*, "The introduction of a new robot for assistance in ophthalmic surgery," in *35th Annual International Conference of the IEEE Engineering in Medicine and Biology Society*, 2013, pp. 5682–5685. DOI: 10.1109/EMBC.2013.6610840.

[13] M. Balicki, J.-H. Han, I. Iordachita, *et al.*, "Single fiber optical coherence tomography microsurgical instruments for computer and robot-assisted retinal surgery," in *Medical Image Computing and Computer-Assisted Intervention – MICCAI*, 2009, pp. 108–115. DOI: 10.1007/978-3-642-04268-3_14.

[14] N. Piccinelli, F. Vesentini, M. Briel, *et al.*, "A shared control architecture for vitreoretinal surgery with safety guarantee using control barrier functions," *Robotics and Automation Letters*, vol. 11, no. 3, pp. 2778–2785, 2026. DOI: 10.1109/LRA.2026.3655284.

[15] M. Briel, D. Wu, M. Hess, *et al.*, "Distance-based shared control for vitreoretinal surgery," *Robotics and Automation Letters*, vol. 11, no. 2, pp. 1858–1865, 2026. DOI: 10.1109/LRA.2025.3641113.

[16] S. Yang, L. A. Lobes Jr, J. N. Martel, and C. N. Riviere, "Handheld-automated microsurgical instrumentation for intraocular laser surgery," *Lasers in Surgery and Medicine*, vol. 47, no. 8, pp. 658–668, 2015. DOI: https://doi.org/10.1002/lsm.22383.

[17] S. Yang, R. A. MacLachlan, J. N. Martel, L. A. Lobes, and C. N. Riviere, "Comparative evaluation of handheld robot-aided intraocular laser surgery," *IEEE Transactions on Robotics*, vol. 32, no. 1, pp. 246–251, 2016. DOI: 10.1109/TRO.2015.2504929.

[18] S. Yang, R. A. MacLachlan, and C. N. Riviere, "Toward automated intraocular laser surgery using a handheld micromanipulator," in *IEEE/RSJ International Conference on Intelligent Robots and Systems*, 2014, pp. 1302–1307. DOI: 10.1109/IROS.2014.6942725.

[19] S. Yang, J. N. Martel, L. A. LobesJr, and C. N. Riviere, "Techniques for robot-aided intraocular surgery using monocular vision," *The International Journal of Robotics Research*, vol. 37, no. 8, pp. 931–952, 2018. DOI: 10.1177/0278364918778352.

[20] S. L. Charreyron, E. Gabbi, Q. Boehler, M. Becker, and B. J. Nelson, "A magnetically steered endolaser probe for automated panretinal photocoagulation," *IEEE Robotics and Automation Letters*, vol. 4, no. 2, 2019. DOI: 10.1109/LRA.2018.2888894.

[21] M. Briel, L. Haide, J. Emmrich, *et al.*, "Intraoperative 3D reconstruction and geometric modeling using sensorized microsurgical instruments," *IEEE Transactions on Medical Robotics and Bionics*, vol. 7, no. 4, pp. 1479–1488, 2025. DOI: 10.1109/TMRB.2025.3604119.

[22] S. Lee and J. Kang, "CNN-based CP-OCT sensor integrated with a subretinal injector for retinal boundary tracking and injection guidance," *Journal of Biomedical Optics*, vol. 26, no. 6, 2021. DOI: 10.1117/1.JBO.26.6.068001.

[23] M. Briel, L. Haide, T. Weber, *et al.*, "Intraoperative fusion of models and data for robust distance sensing," *International Journal of Computer-Assisted Radiology and Surgery*, 2026. DOI: 10.1007/s11548-026-03574-7.

[24] M. Briel, L. Haide, M. Reincke, *et al.*, "Robust distance estimation with out-of-distribution detection in ophthalmic surgery," *IEEE Transactions on Biomedical Engineering*, 2026. DOI: 10.1109/TBME.2026.3661297.

[25] M. Briel, L. Haide, M. Meyling, *et al.*, "Curvature-corrected retinal registration of diagnostic OCT with instrument-integrated OCT," *Scientific Reports*, vol. 15, p. 42 933, 2025. DOI: 10.1038/s41598-025-28922-6.

[26] P. Cornelissen, M. Ourak, G. Borghesan, D. Reynaerts, and E. V. Poorten, "Towards real-time estimation of a spherical eye model based on a single fiber OCT," in *2019 19th International Conference on Advanced Robotics (ICAR)*, 2019, pp. 666–672. DOI: 10.1109/ICAR46387.2019.8981620.

[27] D. Zhou, H. Takeyama, S. Nakao, K. Sonoda, and K. Tadano, "Real-time fundus reconstruction and intraocular mapping using an ophthalmic endoscope," *The International Journal of Medical Robotics and Computer Assisted Surgery*, vol. 19, no. 3, p. 2496, 2023. DOI: 10.1002/rcs.2496.

[28] M. Briel, L. Haide, M. Hess, *et al.*, "Intraoperative adaptive eye model based on instrument-integrated OCT for robot-assisted vitreoretinal surgery," *International Journal of Computer-Assisted Radiology and Surgery*, vol. 20, pp. 881–889, 2025. DOI: 10.1007/s11548-025-03325-0.

[29] P. Zhang, J. W. Kim, P. L. Gehlbach, I. I. Iordachita, and M. Kobilarov, "Autonomous needle navigation in retinal microsurgery: Evaluation in ex vivo porcine eyes," *2023 IEEE International Conference on Robotics and Automation (ICRA)*, pp. 4661–4667, 2023. DOI: 10.1109/icra48891.2023.10161151.

[30] C. F. F. Karney, "Algorithms for geodesics," *Journal of Geodesy*, vol. 87, pp. 43–55, 2013. DOI: 10.1007/s00190-012-0578-z.

[31] D. Liu and J. Nocedal, "On the limited memory BFGS method for large scale optimization," *Mathematical Programming*, vol. 45, pp. 503–528, 1989. DOI: 10.1007/BF01589116.

[32] D. A. Atchison, N. Pritchard, K. L. Schmid, D. H. Scott, C. E. Jones, and J. M. Pope, "Shape of the retinal surface in emmetropia and myopia," *Investigative Ophthalmology & Visual Science*, vol. 46, no. 8, pp. 2698–2707, 2005. DOI: 10.1167/iovs.04-1506.

[33] F.-Y. Lin, C. Bergeles, and G.-Z. Yang, "Biometry-based concentric tubes robot for vitreoretinal surgery," *37th Annual International Conference of the IEEE Engineering in Medicine and Biology Society*, vol. 2015, pp. 5280–5284, 2015. DOI: 10.1109/EMBC.2015.7319583.

[34] O. Caravaca-Mora, P. Zanne, G. Liao, *et al.*, "Automatic intraluminal scanning with a steerable endoscopic optical coherence tomography catheter for gastroenterology applications," *Journal of Optical Microsystems*, vol. 3, no. 1, p. 011 005, 2023. DOI: 10.1117/1.JOM.3.1.011005.